

Cosmological Constraints From the 100 Square Degree Weak Lensing Survey[†]

Jonathan Benjamin^{1†}, Catherine Heymans^{1,2,3}, Elisabetta Semboloni^{2,4},
 Ludovic Van Waerbeke¹, Henk Hoekstra⁵, Thomas Erben⁴, Michael D. Gladders⁶,
 Marco Hetterscheidt⁴, Yannick Mellier^{2,4,7} & H.K.C. Yee⁸

¹ University of British Columbia, 6224 Agricultural Road, Vancouver, V6T 1Z1, B.C., Canada.

² Institut d’Astrophysique de Paris, UMR7095 CNRS, Université Pierre & Marie Curie - Paris, 98 bis bd Arago, 75014 Paris, France.

³ Centre National de la Recherche Scientifique, 3 rue Michel-Ange, 75794 Paris, France

⁴ Argelander-Institut für Astronomie (AIfA), Universität Bonn, Auf dem Hügel 71, 53121 Bonn, Germany.

⁵ Department of Physics and Astronomy, University of Victoria, Victoria, BC, V8P 5C2, Canada.

⁶ Department of Astronomy & Astrophysics, University of Chicago, Chicago, IL 60637, USA

⁷ Observatoire de Paris, LERMA, 61, avenue de l’Observatoire, 75014 Paris, France.

⁸ Department of Astronomy & Astrophysics, University of Toronto, Toronto, ON, M5S 3H4, Canada

21 March 2007

ABSTRACT

We present a cosmic shear analysis of the 100 square degree weak lensing survey, combining data from the CFHTLS-Wide, RCS, VIRMOS-DESCART and GaBoDS surveys. Spanning ~ 100 square degrees, with an average source redshift $z \sim 0.8$, this combined survey allows us to place tight joint constraints on the matter density parameter Ω_m , and the amplitude of the matter power spectrum σ_8 , finding $\sigma_8(\frac{\Omega_m}{0.24})^{0.59} = 0.84 \pm 0.07$. Tables of the measured shear correlation function and the calculated covariance matrix for each survey are included.

The accuracy of our results are a marked improvement on previous work owing to three important differences in our analysis; we correctly account for cosmic variance errors by including a non-Gaussian contribution estimated from numerical simulations; we correct the measured shear for a calibration bias as estimated from simulated data; we model the redshift distribution, $n(z)$, of each survey from the largest deep photometric redshift catalogue currently available from the CFHTLS-Deep. This catalogue is randomly sampled to reproduce the magnitude distribution of each survey with the resulting survey dependent $n(z)$ parametrised using two different models. While our results are consistent for the $n(z)$ models tested, we find that our cosmological parameter constraints depend weakly (at the 5% level) on the inclusion or exclusion of galaxies with low confidence photometric redshift estimates ($z > 1.5$). These high redshift galaxies are relatively few in number but contribute a significant weak lensing signal. It will therefore be important for future weak lensing surveys to obtain near-infra-red data to reliably determine the number of high redshift galaxies in cosmic shear analyses.

Key words: cosmology: cosmological parameters - gravitational lenses - large-scale structure of Universe - observations

1 INTRODUCTION

Weak gravitational lensing of distant galaxies by intervening matter provides a unique and unbiased tool to study the matter distribution

of the Universe. Large scale structure in the Universe induces a weak lensing signal, known as cosmic shear. This signal provides a direct measure of the projected matter power spectrum over a redshift range determined by the lensed sources and over scales ranging from the linear to non-linear regime. The unambiguous interpretation of the weak lensing signal makes it a powerful tool for measuring cosmological parameters which complement those from other probes such as, CMB anisotropies (Spergel et al., 2006) and type Ia supernovae (Astier et al., 2006).

Cosmic shear has only recently become a viable tool for observational cosmology, with the first measurements reported

[†] Based on observations obtained at the Canada-France-Hawaii Telescope (CFHT) which is operated by the National Research Council of Canada (NRCC), the Institut des Sciences de l’Univers (INSU) of the Centre National de la Recherche Scientifique (CNRS) and the University of Hawaii (UH)

† jonben@phas.ubc.ca

simultaneously in 2000 (Bacon et al., 2000; Kaiser et al., 2000; Van Waerbeke et al., 2000; Wittman et al., 2000). The data these early studies utilised were not optimally suited for the extraction of a weak lensing signal. Often having a poor trade off between sky coverage and depth, and lacking photometry in more than one colour, the ability of these early surveys to constrain cosmology via weak lensing was limited, but impressive based on the data at hand. Since these early results several large dedicated surveys have detected weak lensing by large-scale structure, placing competitive constraints on cosmological parameters (Hoekstra et al., 2002a; Bacon et al., 2003; Jarvis et al., 2003; Brown et al., 2003; Hamana et al., 2003; Massey et al., 2005; Rhodes et al., 2004; Van Waerbeke et al., 2005; Heymans et al., 2005; Semboloni et al., 2006; Hoekstra et al., 2006; Schrabback et al., 2006). With the recent first measurements of a changing lensing signal as a function of redshift Bacon et al. (2005); Wittman (2005); Semboloni et al. (2006); Massey et al. (2007b), and the first weak lensing constraints on dark energy Jarvis et al. (2006); Kitching et al. (2006); Hoekstra et al. (2006), the future of lensing is promising.

There are currently several ‘next generation’ surveys being conducted. Their goal is to provide multi-colour data and excellent image quality, over a wide field of view. Such data will enable weak lensing to place tighter constraints on cosmology, breaking the degeneracy between the matter density parameter Ω_m and the amplitude of the matter power spectrum σ_8 and allowing for competitive constraints on dark energy. In this paper, we present a weak lensing analysis of the 100 deg² WL survey that combines data from four of the largest surveys analysed to date, including the wide component of the Canada-France-Hawaii Telescope Legacy Survey (CFHTLS-Wide, Hoekstra et al., 2006), the Garching-Bonn Deep Survey (Ga-BoDs, Hettmansperger et al., 2006), the Red-Sequence Cluster Survey (RCS Hoekstra et al., 2002a), and the VIRMOS-DESCART survey (VIRMOS, Van Waerbeke et al., 2005). These surveys have a combined sky coverage of 113 deg² (96.5 deg², after masking), making this study the largest of its kind.

Our goal in this paper is to provide the best estimates of cosmology currently attainable by weak lensing, through a homogeneous analysis of the major data sets available. Our analysis is distinguished from previous work in three important ways. For the first time we account for the effects of non-Gaussian contributions to the analytic estimate of the cosmic variance covariance matrix (Schneider et al., 2002), as described in Semboloni et al. (2007). Results from the Shear TEsting Programme (STEP, see Massey et al., 2007a; Heymans et al., 2006a) are used to correct for calibration error in our shear measurement methods, a marginalisation over the uncertainty in this correction is performed. We use the largest deep photometric redshift catalogue currently available (Ilbert et al., 2006), which provides redshifts for ~ 500000 galaxies in the CFHTLS-Deep. Additionally, we properly account for cosmic variance in our calculation of the redshift distribution, an important source of error discussed in Van Waerbeke et al. (2006).

This paper is organised as follows: in §2 we give a short overview of cosmic shear theory, and outline the relevant statistics used in this work. We describe briefly each of the surveys used in this study in §3. We present the measured shear signal in §4. In §5 we present the derived redshift distributions for each survey. We present the results of the combined parameter estimation in §6, closing thoughts and future prospects are discussed in §7.

2 COSMIC SHEAR THEORY

We briefly describe here the notations and statistics used in our cosmic shear analysis. For detailed reviews of weak lensing theory the reader is referred to Munshi et al. (2006), Bartelmann & Schneider (2001), and Schneider et al. (1998). The notations used in the latter are adopted here. The power spectrum of the projected density field (convergence κ) is defined as

$$P_\kappa(k) = \frac{9 H_0^4 \Omega_m^2}{4c^4} \int_0^{w_H} \frac{dw}{a^2(w)} P_{3D} \left(\frac{k}{f_K(w)}; w \right) \times \left[\int_w^{w_H} dw' n(w') \frac{f_K(w' - w)}{f_K(w')} \right]^2, \quad (1)$$

where H_0 is the Hubble constant, $f_K(w)$ is the comoving angular diameter distance out to a distance w (w_H is the comoving horizon distance), and $n[w(z)]$ is the redshift distribution of the sources (see §5). P_{3D} is the 3-dimensional mass power spectrum computed from a non-linear estimation of the dark matter clustering (see for example Peacock & Dodds, 1996; Smith et al., 2003), and k is the 2-dimensional wave vector perpendicular to the line-of-sight.

In this paper we focus on the shear correlation function statistic ξ . For a galaxy pair separation θ , we define

$$\begin{aligned} \xi_+(\theta) &= \langle \gamma_t(r) \gamma_t(r + \theta) \rangle + \langle \gamma_r(r) \gamma_r(r + \theta) \rangle, \\ \xi_-(\theta) &= \langle \gamma_t(r) \gamma_t(r + \theta) \rangle - \langle \gamma_r(r) \gamma_r(r + \theta) \rangle, \end{aligned} \quad (2)$$

where the shear $\gamma = (\gamma_t, \gamma_r)$ is rotated into the local frame of the line joining the centres of each galaxy pair separated by θ . The shear correlation function ξ_+ is related to the convergence power spectrum through

$$\xi_+(\theta) = \frac{1}{2\pi} \int_0^\infty dk k P_\kappa(k) J_0(k\theta). \quad (3)$$

A quantitative measurement of the lensing amplitude and the systematics is obtained by splitting the signal into its curl-free (E -mode) and curl (B -mode) components respectively. This method has been advocated to help the measurement of the intrinsic alignment contamination in the weak lensing signal (Crittenden et al., 2001, 2002), but it is also an efficient measure of the residual systematics from the PSF correction (Pen et al., 2002).

The E and B modes derived from the shape of galaxies are unambiguously defined only for the so-called aperture mass variance $\langle M_{ap}^2 \rangle$, which is a weighted shear variance within a cell of radius θ_c . The cell itself is defined as a compensated filter, such that a constant convergence κ gives $M_{ap} = 0$. $\langle M_{ap}^2 \rangle$ can be rewritten as a function of the tangential shear γ_t if we express $\gamma = (\gamma_t, \gamma_r)$ in the local frame of the line connecting the aperture centre to the galaxy. $\langle M_{ap}^2 \rangle$ is given by:

$$\langle M_{ap}^2 \rangle = \frac{288}{\pi \theta_c^4} \int_0^\infty \frac{dk}{k^3} P_\kappa(k) [J_4(k\theta_c)]^2. \quad (4)$$

The B -mode $\langle M_{ap}^2 \rangle_\perp$ is obtained by replacing γ_t with γ_r . The aperture mass is insensitive to the mass sheet degeneracy, and therefore it provides an unambiguous splitting of the E and B modes. The drawback is that aperture mass is a much better estimate of the small scale power than the large scale power which can be seen from the function $J_4(k\theta_c)$ in Eq.(4) which peaks at $k\theta_c \sim 5$. Essentially, all scales larger than a fifth of the largest survey scale remain inaccessible to M_{ap} . The large-scale part of the lensing signal is lost by M_{ap} , while the remaining small-scale fraction is difficult to interpret because the strongly non-linear power is difficult to predict accurately (Van Waerbeke et al., 2002). It is therefore prefer-

able to decompose the shear correlation function into its E and B modes, as it is a much deeper probe of the linear regime.

Following Crittenden et al. (2001, 2002), we define

$$\xi'(\theta) = \xi_-(\theta) + 4 \int_{\theta}^{\infty} \frac{d\vartheta}{\vartheta} \xi_-(\vartheta) - 12\theta^2 \int_{\theta}^{\infty} \frac{d\vartheta}{\vartheta^3} \xi_-(\vartheta). \quad (5)$$

The E and B shear correlation functions are then given by

$$\xi_E(\theta) = \frac{\xi_+(\theta) + \xi'(\theta)}{2}, \quad \xi_B(\theta) = \frac{\xi_+(\theta) - \xi'(\theta)}{2}. \quad (6)$$

In the absence of systematics, $\xi_B = 0$ and $\xi_E = \xi_+$ (Eq.3). In contrast with the M_{ap} statistics, the separation of the two modes depends on the signal integrated outwith the scales probed by all surveys. One option is to calculate Eq.(6) using a fiducial cosmology to compute ξ_- on scales $\theta \rightarrow \infty$. As shown in Heymans et al. (2005), changes in the choice of fiducial cosmology does not significantly effect the results, allowing this statistic to be used as a diagnostic tool for the presence of systematics. This option does however prevent us from using ξ_E to constrain cosmology. As the statistical noise on the measured ξ_E is $\sim \sqrt{2}$ smaller than the statistical noise on the measured ξ_+ , there is a more preferable alternative. If the survey size is sufficiently large in comparison to the scales probed by ξ_E , we can consider the unknown integral to be a constant that can be calibrated using the aperture mass B -mode statistic $\langle M_{ap}^2(\Delta\theta) \rangle_{\perp}$. A range $\Delta\theta$ of angular scales where $\langle M_{ap}^2(\Delta\theta) \rangle_{\perp} \sim 0$ ensures that the B -mode of the shear correlation function is zero as well (within the error bars), at angular scales $\sim \frac{\Delta\theta}{3}$. In this analysis we have calibrated $\xi_{E,B}$ for our survey data in this manner. This alternative method has also been verified by recalculating $\xi_{E,B}$ using our final best-fit cosmology to extrapolate the signal. We find the two methods to be in very close agreement.

3 DATA DESCRIPTION

In this section we summarise the four weak lensing surveys that form the 100 deg² WL survey: CFHTLS-Wide (Hoekstra et al., 2006), GaBoDs (Hetzterscheidt et al., 2006), RCS (Hoekstra et al., 2002a), and VIRMOS-DESCART (Van Waerbeke et al., 2005), see Table 1 for an overview. Note that we have chosen not to include the CFHTLS-Deep data (Semboloni et al., 2006) in this analysis since the effective area of the analysed data is only 2.3 deg². Given the breadth of the parameter constraints obtained from this preliminary data set there is little value to be gained by combining it with four surveys which are among the largest available.

3.1 CFHTLS-Wide

The Canada-France-Hawaii Telescope Legacy Survey (CFHTLS) is a joint Canadian-French program designed to take advantage of Megaprime, the CFHT wide-field imager. This 36 CCD mosaic camera has a 1×1 degree field of view and a resolution of 0.187 arcseconds per pixel. The CFHTLS has been allocated ~ 450 nights over a 5 year period (starting in 2003), the goal is to complete three independent survey components; deep, wide, and very wide. The wide component will be imaged with five broad-band filters: u^* , g^* , r^* , i^* , z^* . With the exception of u^* these filters are designed to match the SDSS photometric system (Fukugita et al., 1996). The three wide fields will span a total of 170 deg² on completion. In this study, as in Hoekstra et al. (2006), we use data from the W1 and W3 fields that total 22 deg² after masking, and reach a depth of $i^* = 24.5$. For detailed information concerning data reduction and

object analysis the reader is referred to Hoekstra et al. (2006), and Van Waerbeke et al. (2002).

3.2 GaBoDS

The Garching-Bonn Deep Survey (GaBoDS) data set was obtained with the Wide Field Imager (WFI) of the MPG/ESO 2.2m telescope on La Silla, Chile. The camera consists of 8 CCDs with a 34 by 33 arcminute field of view and a resolution of 0.238 arcseconds per pixel. The total data set consists of 52 statistically independent fields, with a total effective area (after trimming) of 13 deg². The magnitude limits of each field ranges between $R_{VEGA} = 25.0$ and $R_{VEGA} = 26.5$ (this corresponds to a 5 σ detection in a 2 arcsecond aperture). To obtain a homogeneous depth across the survey we follow Hetterscheidt et al. (2006) performing our lensing analysis with only those objects which lie in the complete magnitude interval $R \in [21.5, 24.5]$. For further details of the data set, and technical information regarding the reduction pipeline the reader is referred to Hetterscheidt et al. (2006).

3.3 VIRMOS-DESCART

The DESCART weak lensing project is a theoretical and observational program for cosmological weak lensing investigations. The cosmic shear survey carried out by the DESCART team uses the CFH12k data jointly with the VIRMOS survey to produce a large homogeneous photometric sample in the $BVRI$ broad band filters. CFH12k is a 12 CCD mosaic camera mounted at the Canada-France-Hawaii Telescope prime focus, with a 42 by 28 arcminute field of view and a resolution of 0.206 arcseconds per pixel. The VIRMOS-DESCART data consist of four uncorrelated patches of 2 × 2 deg² separated by more than 40 degrees. Here, as in Van Waerbeke et al. (2005), we use I_{AB} -band data from all four fields, which have an effective area of 8.5 deg² after masking, and a limiting magnitude of $I_{AB} = 24.5$ (this corresponds to a 5 σ detection in a 3 arcsecond aperture). Technical details of the data set are given in Van Waerbeke et al. (2001) and McCracken et al. (2003), while an overview of the VIRMOS-DESCART survey is given in Le Fèvre et al. (2004).

3.4 RCS

The Red-Sequence Cluster Survey (RCS) is a galaxy cluster survey designed to provide a large sample of optically selected clusters of galaxies with redshifts between 0.3 and 1.4. The final survey covers 90 deg² in both R_C and z' , spread over 22 widely separated patches of $\sim 2.1 \times 2.3$ degrees. The northern half of the survey was observed using the CFH12k camera on the CFHT, and the southern half using the Mosaic II camera mounted at the Cerro Tololo Inter-American Observatory (CTIO), Victor M. Blanco 4m telescope prime focus. This camera has an 8 CCD wide field imager with a 36 by 36 arcminute field of view and a resolution of 0.27 arcseconds per pixel. The data studied here, as in Hoekstra et al. (2002a), consist of a total effective area of 53 deg² of masked imaging data, spread over 13 patches, with a limiting magnitude of 25.2 (corresponding to a 5 σ point source depth) in the R_C band. 43 deg² were taken with the CFHT, the remaining 10 deg² were taken with the Blanco telescope. A detailed description of the data reduction and object analysis is described in Hoekstra et al. (2002b), to which we refer for technical details.

Table 1. Summary of the published results from each survey used in this study. The values for σ_8 correspond to $\Omega_m = 0.24$, and are given for the Peacock & Dodds (1996) method of calculating the non-linear evolution of the matter power spectrum. The statistics listed were used in the previous analyses; the shear correlation functions $\xi_{E,B}$ (Eq. 6), the aperture mass statistic $\langle M_{ap}^2 \rangle$ (Eq. 4) and the top-hat shear variance $\langle \gamma_{E,B}^2 \rangle$ (see Van Waerbeke et al. (2005)).

	CFHTLS-Wide	GaBoDS	RCS	VIRMOS-DESCART
Area (deg ²)	22.0	13.0	53	8.5
N _{fields}	2	52	13	4
Magnitude Range	$21.5 < i' < 24.5$	$21.5 < R < 24.5$	$22 < R_C < 24$	$21 < I_{AB} < 24.5$
$\langle z_{\text{source}} \rangle$	0.81	0.78	~ 0.6	0.92
Previous Analysis	Hoekstra et al. (2006)	Hetterscheidt et al. (2006)	Hoekstra et al. (2002a)	Van Waerbeke et al. (2005)
$\sigma_8 (\Omega_m = 0.24)$	0.99 ± 0.07	0.92 ± 0.13	0.98 ± 0.16	0.96 ± 0.08
Statistic	$\xi_{E,B}(\theta)$	$\langle M_{ap}^2 \rangle(\theta)$	$\langle M_{ap}^2 \rangle(\theta)$	$\langle \gamma_{E,B}^2 \rangle(\theta)$

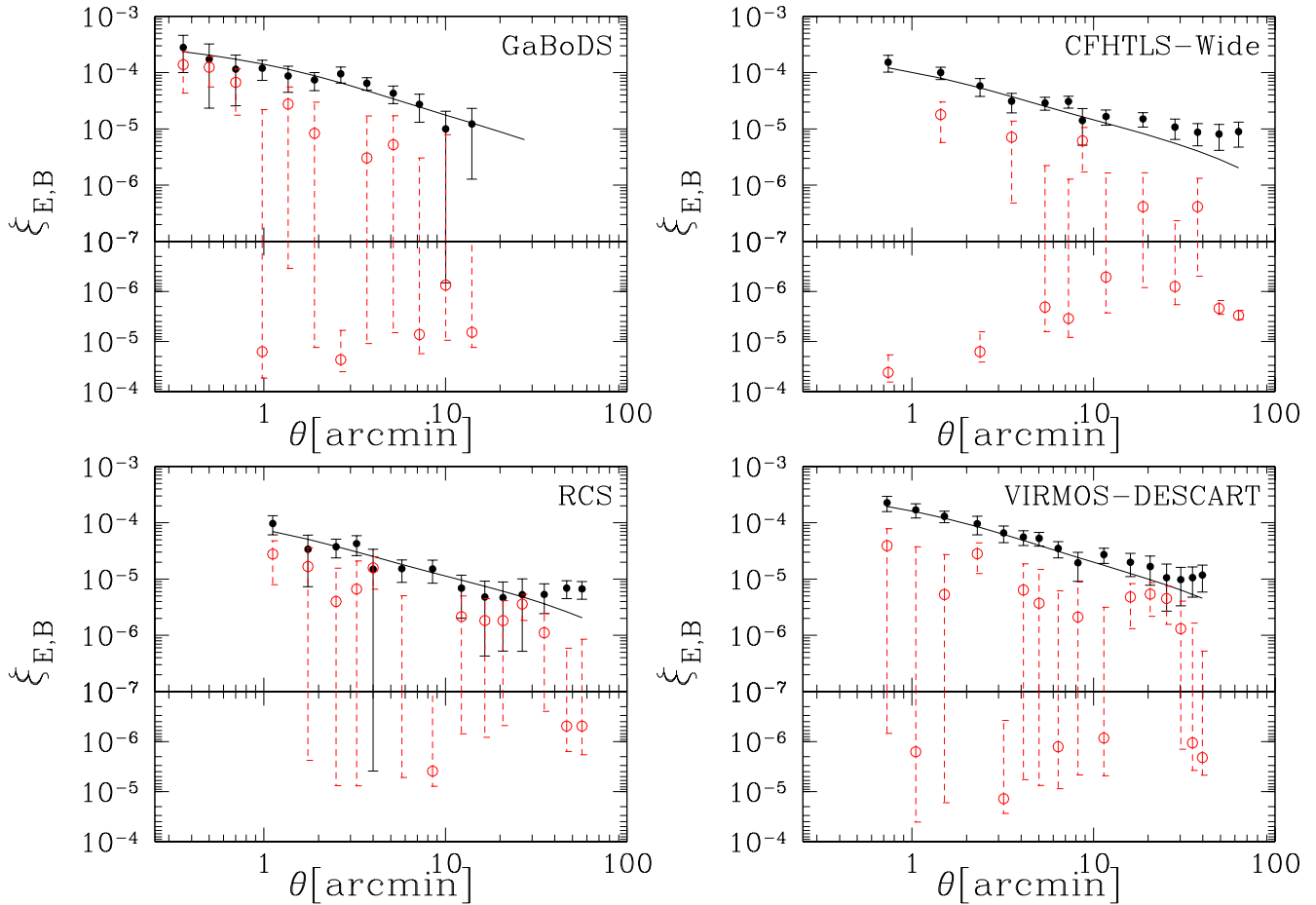


Figure 1. E and B modes of the shear correlation function ξ (filled and open points, respectively) as measured for each survey. Note that the 1σ errors on the E -modes include statistical noise, non-Gaussian cosmic variance (see §6) and a systematic error given by the magnitude of the B -mode. The 1σ error on the B -modes is statistical only. The results are presented on a log-log scale, despite the existence of negative B -modes. We have therefore collapsed the infinite space between 10^{-7} and zero, and plotted negative values on a separate log scale mirrored on 10^{-7} . Hence all values on the lower portion of the graph are negative, their absolute value is given by the scaling of the graph. Note that this choice of scaling exaggerates any discrepancies. The solid lines show the best fit Λ CDM model for $\Omega_m = 0.24$, $h = 0.72$, $\Gamma = h\Omega_m$, σ_8 given in Table 4, and $n(z)$ given in Table 2. The latter two being chosen for the case of the high confidence redshift calibration sample, an $n(z)$ modeled by Eq.(9), and the non-linear power spectrum estimated by Smith et al. (2003).

4 COSMIC SHEAR SIGNAL

Lensing shear has been measured for each survey using the common KSB galaxy shape measurement method (Kaiser et al., 1995; Luppino & Kaiser, 1997; Hoekstra et al., 1998). The practical application of this method to the four surveys differs slightly, as tested by the Shear TEsting Programme; STEP (Massey et al., 2007a; Heymans et al., 2006a), resulting in a small calibration bias in the measurement of the shear. Heymans et al. (2006a) define both a calibration bias (m) and an offset of the shear (c),

$$\gamma_{\text{meas}} - \gamma_{\text{true}} = m\gamma_{\text{true}} + c, \quad (7)$$

where γ_{meas} is the measured shear, γ_{true} is the true shear signal, and m and c are determined from an analysis of simulated data. As the value of c is highly dependent on the strength of the PSF distribution we take $c = 0$, which for our purposes is a very good approximation. Eq.(7) then simplifies to $\gamma_{\text{true}} = \gamma_{\text{meas}}(m+1)^{-1}$. The calibration bias for the CFHTLS-Wide, RCS and VIRMOS-DESCART (HH analysis in Massey et al. (2007a)) is $m = -0.0017 \pm 0.0088$, and $m = 0.038 \pm 0.026$ for GaBoDS (MH analysis in Massey et al. (2007a)).

We measure the shear correlation functions $\xi_E(\theta)$ and $\xi_B(\theta)$ (Eq. 6) for each survey, shown in Figure 1. As discussed in §2, these statistics are calibrated using the measured aperture mass B -mode $\langle M_{\text{ap}}^2 \rangle_{\perp}$. The 1σ errors on ξ_E include statistical noise, computed as described in Schneider et al. (2002), non-Gaussian cosmic variance (see §6 for details), and a systematic error added in quadrature. The systematic error for each angular scale θ is given by the magnitude of $\xi_B(\theta)$. The 1σ errors on ξ_B are statistical only. We correct for the calibration bias by scaling ξ_E by $(1+m)^{-2}$, the power of negative 2 arising from the fact that ξ_E is a second order shear statistic. Tables containing the measured correlation functions and their corresponding covariance matrix can be found in appendix A. When estimating parameter constraints in §6.2 we marginalise over the error on the calibration bias (stated above), which expresses the range of admissible scalings of ξ_E .

5 REDSHIFT DISTRIBUTION

The measured weak lensing signal depends on the redshift distribution of the sources, as seen from Eq.(1). Past weak lensing studies (e.g., Hoekstra et al. (2006); Semboloni et al. (2006); Massey et al. (2005); Van Waerbeke et al. (2005)) have used the Hubble Deep Field (HDF) photometric redshifts to estimate the shape of the redshift distribution. Spanning only 5.3 arcmin², the HDF suffers from cosmic variance as described in Van Waerbeke et al. (2006), where it is also suggested that the HDF fields may be subject to a selection bias. This cosmic variance on the measured redshift distribution adds an additional error into the weak lensing analysis that is not typically accounted for.

In this study we use the largest deep photometric redshift catalogue in existence, from Ilbert et al. (2006), who have estimated redshifts on the four Deep fields of the T0003 CFHTLS release. The redshift catalogue is publicly available at *terapix.iap.fr*. The full photometric catalogue contains 522286 objects, covering an effective area of 3.2 deg². A set of 3241 spectroscopic redshifts with $0 \leq z \leq 5$ from the VIRMOS VLT Deep Survey (VVDS) were used as a calibration and training set for the photometric redshifts. The resulting photometric redshifts have an accuracy of $\sigma_{\Delta z/1+z_s} = 0.043$ for $i'_{\text{AB}} = 22.5 - 24$, with a fraction of catastrophic errors of 5.4%. Ilbert et al. (2006) demonstrate that their

derived redshifts work best in the range $0.2 \leq z \leq 1.5$, having a fraction of catastrophic errors of $\sim 5\%$ in this range. The fraction of catastrophic errors increases dramatically at $z < 0.2$ and $1.5 < z < 3$ reaching $\sim 40\%$ and $\sim 70\%$ respectively. This is explained by a degeneracy between galaxies at $z_{\text{spec}} < 0.4$ and $1.5 < z_{\text{phot}} < 3$ due to a mismatch between the Balmer break and the intergalactic Lyman-alpha forest depression.

Van Waerbeke et al. (2006) estimate the expected sampling error on the average redshift for such a photometric redshift sample to be $\sim 3\%/\sqrt{4} = 1.5\%$, where the factor of $\sqrt{4}$ comes from the four independent CFHTLS-Deep fields, a great improvement over the $\sim 10\%$ error expected for the HDF sample.

5.1 Magnitude Conversions

In order to estimate the redshift distributions of the surveys, we calibrate the magnitude distribution of the photometric redshift sample (hence forth the z_p sample) to that of a given survey by converting the CFHTLS filter set $u^*g'r'i'z'$ to I_{AB} magnitudes for VIRMOS and R_{VEGA} magnitudes for RCS and GaBoDs. We employ the linear relationships between different filter bands given by Blanton & Roweis (2007):

$$I_{\text{AB}} = i' - 0.0647 - 0.7177 [(i' - z') - 0.2083], \quad (8)$$

$$R_{\text{VEGA}} = r' - 0.0576 - 0.3718 [(r' - i') - 0.2589] - 0.21.$$

These conversions were estimated by fitting spectral energy distribution templates to data from the Sloan Digital Sky Survey. They are considered to be accurate to 0.05 mag or better, and are thus good enough for our purposes.

5.2 Modeling the redshift distribution $n(z)$

The galaxy weights used in each survey's lensing analysis result in a weighted source redshift distribution. To estimate the effective $n(z)$ of each survey we draw galaxies at random from the z_p sample, using the method described in §6.5.1 of Wall & Jenkins (2003) to reproduce the shape of the weighted magnitude distribution of each survey. A Monte Carlo (bootstrap) approach is taken to account for the errors in the photometric redshifts, as well as the statistical variations expected from drawing a random sample of galaxies from the z_p sample to create the redshift distribution. The process of randomly selecting galaxies from the z_p sample, and therefore estimating the redshift distribution of the survey, is repeated 1000 times. Each redshift that is selected is drawn from its probability distribution defined by the ± 1 and $\pm 3\sigma$ errors (since these are the error bounds given in Ilbert et al. (2006)'s catalogue). The sampling of each redshift is done such that a uniformly random value within the 1σ error is selected 68% of the time, and a uniformly random value within the three sigma error (but exterior to the 1σ error) is selected 32% of the time. The redshift distribution is then defined as the average of the 1000 constructions, and an average covariance matrix of the redshift bins is calculated.

At this point cosmic variance and Poisson noise are added to the diagonal elements of the covariance matrix, following Van Waerbeke et al. (2006). They provide a scaling relation between cosmic (sample) variance noise and Poisson noise where $\sigma_{\text{sample}}/\sigma_{\text{Poisson}}$ is given as a function of redshift for different sized calibration samples. We take the curve for a 1 deg² survey, the size of a single CFHTLS-Deep field, and divide by $\sqrt{4}$ since

Table 2. The best fit model parameters for the redshift distribution, given by either Eq.(9) or Eq.(10). Models are fit using the full calibration sample of Ilbert et al. (2006) $0.0 \leq z_p \leq 4.0$, and using only the high confidence region $0.2 \leq z_p \leq 1.5$. χ^2_ν is the reduced χ^2 statistic, $\langle z \rangle$, and z_m are the average and median redshift respectively, calculated from the model on the range $0.0 \leq z \leq 4.0$.

Eq.(9)												Eq.(10)			
0.2 $\leq z_p \leq 1.5$	CFHTLS-Wide	α	β	z_0	$\langle z \rangle$	z_m	χ^2_ν	a	b	c	N	$\langle z \rangle$	z_m	χ^2_ν	
	GaBoDS	0.836	3.425	1.171	0.802	0.788	1.63	0.723	6.772	2.282	2.860	0.848	0.812	1.65	
	RCS	0.700	3.186	1.170	0.784	0.760	1.96	0.571	6.429	2.273	2.645	0.827	0.784	2.80	
	VIRMOS-DESCART	0.787	3.436	1.157	0.781	0.764	1.41	0.674	6.800	2.095	2.642	0.823	0.788	1.60	
0.0 $\leq z_p \leq 4.0$	CFHTLS-Wide	0.637	4.505	1.322	0.823	0.820	1.48	0.566	7.920	6.107	6.266	0.859	0.844	2.06	
	GaBoDS	1.197	1.193	0.555	0.894	0.788	8.94	0.740	4.563	1.089	1.440	0.945	0.828	2.41	
	RCS	1.360	0.937	0.347	0.938	0.800	7.65	0.748	3.932	0.800	1.116	0.993	0.832	2.40	
	VIRMOS-DESCART	1.423	1.032	0.391	0.888	0.772	5.67	0.819	4.418	0.800	1.201	0.939	0.808	1.84	

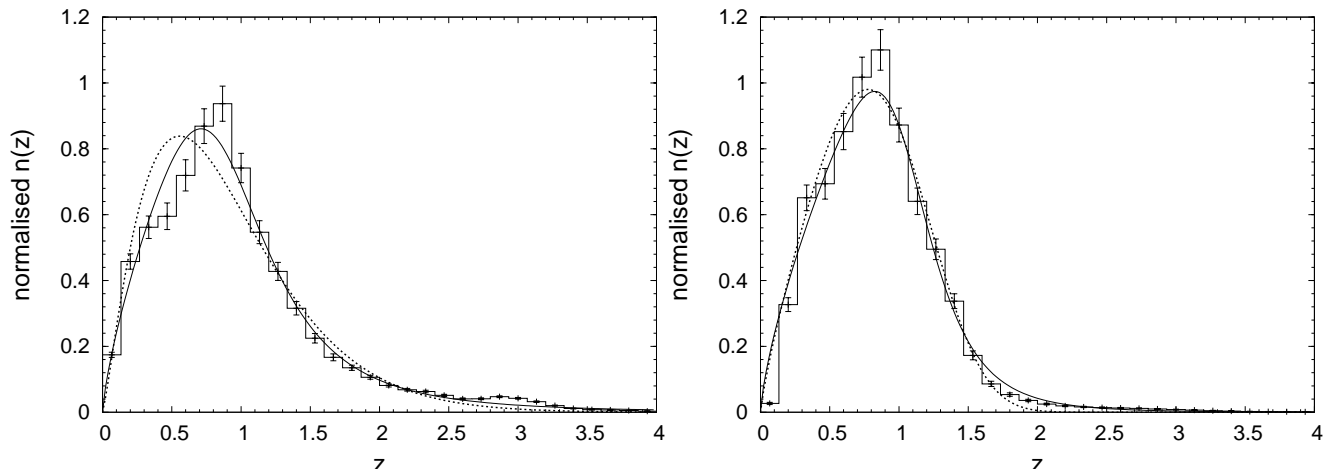


Figure 2. Normalised redshift distribution for the CFHTLS-Wide survey, given by the histogram, where the error bars include Poisson noise and cosmic variance of the photometric redshift sample. The dashed curve shows the best fit for Eq.(9), and the solid curve for Eq.(10). **Left:** Distribution obtained if all photometric redshifts are used $0.0 \leq z \leq 4.0$, and χ^2 is calculated between $0.0 \leq z \leq 2.5$. **Right:** Distribution obtained if only the high confidence redshifts are used $0.2 \leq z \leq 1.5$, and χ^2 is calculated on this range. The existence of counts for $z > 1.5$ is a result of drawing the redshifts from their full probability distributions.

there are four independent 1 deg^2 patches of sky in the photometric redshift sample.

Based on the photometric redshift sample of Ilbert et al. (2006) we consider two redshift ranges, the full range of redshifts in the photometric catalogues $0.0 \leq z \leq 4.0$, and the high confidence range $0.2 \leq z \leq 1.5$. The goal is to assess to what extent this will affect the redshift distribution, and –in turn– the derived parameter constraints.

The shape of the normalised redshift distribution is often assumed to take the following form:

$$n(z) = \frac{\beta}{z_0 \Gamma\left(\frac{1+\alpha}{\beta}\right)} \left(\frac{z}{z_0}\right)^\alpha \exp\left[-\left(\frac{z}{z_0}\right)^\beta\right], \quad (9)$$

where α , β , and z_0 are free parameters. If the full range of photometric redshifts is used the shape of the redshift distribution is poorly fit by Eq.(9), this is a result of the function’s exponential drop off which can not accommodate the number of high redshift galaxies in the tail of the distribution (see Fig.(2)). We therefore

adopt a new function in an attempt to better fit the normalised redshift distribution,

$$n(z) = N \frac{z^a}{z^b + c}, \quad (10)$$

where a , b , and c are free parameters, and N is a normalising factor,

$$N = \left(\int_0^\infty dz' \frac{z'^a}{z'^b + c} \right)^{-1}. \quad (11)$$

The best fit model is determined by minimising the generalised chi square statistic:

$$\chi^2 = (d_i - m_i) \mathbf{C}^{-1} (d_i - m_i)^T, \quad (12)$$

where \mathbf{C} is the covariance matrix of the binned redshift distribution described above, d_i is the data vector, and m_i is the model vector. For each survey we determine the best fit for both Eq.(9) and Eq.(10) in either case we consider both the full range of redshifts and the high confidence range, the results are presented in Table 2.

Figure 2 shows the best fit models to the CFHTLS-Wide survey, when the full range of photometric redshifts is considered (left panel) Eq.(10) clearly fits the distribution better than Eq.(9), having reduced χ^2 statistics of 2.41 and 8.94 respectively. When we consider only the high confidence redshifts (right panel of Figure 2) both functions fit equally well having reduced χ^2 statistics of 1.65 and 1.63 for Eq.(10) and Eq.(9) respectively. Note that the redshift distribution is non-zero at $z > 1.5$ for the high confidence photometric redshifts ($0.2 \leq z_p \leq 1.5$) because of the Monte Carlo sampling of the redshifts from their probability distributions.

6 PARAMETER ESTIMATION

6.1 Maximum likelihood method

We investigate a six dimensional parameter space consisting of the mean matter density Ω_m , the normalisation of the matter power spectrum σ_8 , the Hubble parameter h , and $n(z)$ the redshift distribution parametrised by either α , β , and z_0 (Eq.9) or a , b , and c (Eq.10). A flat cosmology ($\Omega_m + \Omega_\Lambda = 1$) is assumed throughout, and the shape parameter is given by $\Gamma = \Omega_m h$. The default priors are taken to be $\Omega_m \in [0.1, 1]$, $\sigma_8 \in [0.5, 1.2]$, and $h \in [0.64, 0.8]$ with the latter in agreement with the findings of the HST key project (Freedman et al., 2001). The priors on the redshift distribution were arrived at using a Monte Carlo technique. This is necessary since the three parameters of either Eq.(9) or Eq.(10) are very degenerate, hence simply finding the 2 or 3 σ levels of one parameter while keeping the other two fixed at their best fit values does not fairly represent the probability distribution of the redshift parameters. The method used ensures a sampling of parameter triplets whose number count follow the 3-D probability distribution; that is 68% lie within the 1σ volume, 97% within the 2σ volume, etc. We find 100 such parameter trios and use them as the prior on the redshift distribution, therefore this is a Gaussian prior on $n(z)$.

Given the data vector ξ_i , which is the shear correlation function (ξ_E of Eq.6) as a function of scale, and the model prediction $m_i(\Omega_m, \sigma_8, h, n(z))$ the likelihood function of the data is given by

$$\mathcal{L} = \frac{1}{\sqrt{(2\pi)^n |\mathbf{C}|}} \exp \left[-\frac{1}{2} (\xi_i - m_i) \mathbf{C}^{-1} (\xi_i - m_i)^T \right], \quad (13)$$

where n is the number of angular scale bins and \mathbf{C} is the $n \times n$ covariance matrix. The shear covariance matrix can be expressed as

$$C_{ij} = \langle (\xi_i - \mu_i)^T (\xi_j - \mu_j) \rangle, \quad (14)$$

where μ_i is the mean of the shear ξ_i at scale i , and angular brackets denote the average over many independent patches of sky. To obtain a reasonable estimate of the covariance matrix for a given set of data one needs many independent fields, this is not the case for either the CFHTLS-Wide or VIRMOS-DESCART surveys.

We opt to take a consistent approach for all 4 data sets by decomposing the shear covariance matrix as $\mathbf{C} = \mathbf{C}_n + \mathbf{C}_B + \mathbf{C}_s$, where \mathbf{C}_n is the statistical noise, \mathbf{C}_B is the absolute value of the residual B -mode and \mathbf{C}_s is the cosmic variance covariance matrix. \mathbf{C}_n can be measured directly from the data, it represents the statistical noise inherent in a finite data set. \mathbf{C}_B is diagonal and represents the addition of the B -mode in quadrature to the uncertainty, this provides a conservative limit to how well the lensing signal can be determined.

For Gaussian cosmic variance the matrix \mathbf{C}_s can be computed according to Schneider et al. (2002), assuming an effective survey

Table 3. Data used for each survey to calculate the Gaussian contribution to the cosmic variance covariance matrix. A_{eff} is the effective area, n_{eff} the effective galaxy number density, and σ_e the intrinsic ellipticity dispersion.

	A_{eff} (deg ²)	n_{eff} (arcmin ⁻²)	σ_e
CFHTLS-Wide	22	12	0.47
RCS	53	8	0.44
VIRMOS-DESCART	8.5	15	0.44
GaBoDS	13	12.5	0.50

area A_{eff} , an effective number density of galaxies n_{eff} , and an intrinsic ellipticity dispersion σ_e (see Table 3). However, as shown by Semboloni et al. (2007), non-linear effects at small scales lead to significant deviations from Gaussian behaviour. They use ray tracing simulations to determine the effect of non-Gaussian contributions to the cosmic shear covariance matrix, calculating the following:

$$\mathcal{F}(\vartheta_1, \vartheta_2) = \frac{C_{\text{meas}}(\xi_+; \vartheta_1, \vartheta_2)}{C_{\text{Gaus}}(\xi_+; \vartheta_1, \vartheta_2)}, \quad (15)$$

where $\mathcal{F}(\vartheta_1, \vartheta_2)$ is the ratio of the covariance measured from N-body simulations ($C_{\text{meas}}(\xi_+; \vartheta_1, \vartheta_2)$) to that expected from Gaussian effects alone ($C_{\text{Gaus}}(\xi_+; \vartheta_1, \vartheta_2)$). It is found that $\mathcal{F}(\vartheta_1, \vartheta_2)$ increases significantly above unity at scales smaller than 10 arcminutes, the parametrised fit as a function of mean source redshift is given by,

$$\begin{aligned} \mathcal{F}(\vartheta_1, \vartheta_2) &= \frac{p_1(z)}{[\vartheta_1^2 \vartheta_2^2]^{p_2(z)}}, \\ p_1(z) &= \frac{16.9}{z^{0.95}} - 2.19, \\ p_2(z) &= 1.62 z^{-0.68} \exp(-z^{-0.68}) - 0.03. \end{aligned} \quad (16)$$

A fiducial model is required to calculate the Gaussian covariance matrix, it is taken as $\Omega_m = 0.3$, $\Lambda = 0.7$, $\sigma_8 = 0.8$, $h = 0.72$, and the best fit $n(z)$ model (see Table 2). We then use the above prescription at scales less than ~ 10 arcminutes to account for non-Gaussianities. For each survey the total covariance matrix ($\mathbf{C} = \mathbf{C}_n + \mathbf{C}_s + \mathbf{C}_B$) is presented in appendix A.

To test this method we compare our analytic covariance matrix for GaBoDS with that found by measuring it from the data (Hettterscheidt et al., 2006). Since GaBoDS images 52 independent fields it is possible to obtain an estimate of \mathbf{C} directly from the data. The contribution from the B -modes (\mathbf{C}_B) is not added to our analytic estimate in this case, since its inclusion is meant as a conservative estimate of the systematic errors. We find a median percent difference along the diagonal of $\sim 15\%$, which agrees well with the accuracy obtained for simulated data (Semboloni et al., 2007).

6.2 Joint constraints on σ_8 and Ω_m

For the combined survey we place joint constraints on σ_8 and Ω_m as shown in Figure 3. Fitting to the maximum likelihood region we find $\sigma_8 = (0.84 \pm 0.07) (\frac{\Omega_m}{0.24})^{-0.59}$, where the error is the 1σ level for $\Omega_m = 0.24$. This result assumes a flat Λ CDM cosmology and adopts the non-linear matter power spectrum of Smith et al. (2003). The redshift distribution is estimated from the high confidence CFHTLS-Deep photometric redshifts using the standard $n(z)$ model given in Eq.(9). Marginalisation was performed over

Table 4. Joint constraints on the amplitude of the matter power spectrum σ_8 , and the matter energy density Ω_m , parametrised as $\sigma_8 = \beta(\frac{\Omega_m}{0.24})^{-\alpha}$.

		0.0 $\leq z_p \leq 4.0$				0.2 $\leq z_p \leq 1.5$			
		Eq.(9)		Eq.(10)		Eq.(9)		Eq.(10)	
		β	α	β	α	β	α	β	α
Smith et al. (2003)	CFHTLS-Wide	0.84 \pm 0.07	0.55	0.81 \pm 0.06	0.54	0.86 \pm 0.07	0.56	0.84 \pm 0.07	0.55
	GaBoDS	0.93 \pm 0.11	0.60	0.89 \pm 0.09	0.59	1.01 \pm 0.11	0.65	0.98 \pm 0.13	0.63
	RCS	0.75 \pm 0.07	0.55	0.73 \pm 0.08	0.55	0.78 \pm 0.07	0.57	0.76 \pm 0.07	0.56
	VIRMOS-DESCART	0.99 \pm 0.07	0.59	0.95 \pm 0.08	0.58	1.02 \pm 0.08	0.60	1.00 \pm 0.09	0.59
	Combined	0.80 \pm 0.06	0.57	0.77 \pm 0.05	0.56	0.84 \pm 0.07	0.59	0.82 \pm 0.06	0.58
Peacock & Dodds (1996)	CFHTLS-Wide	0.87 \pm 0.08	0.57	0.83 \pm 0.07	0.56	0.89 \pm 0.08	0.58	0.87 \pm 0.08	0.57
	GaBoDS	0.96 \pm 0.10	0.62	0.93 \pm 0.10	0.60	1.04 \pm 0.12	0.66	1.01 \pm 0.11	0.64
	RCS	0.77 \pm 0.07	0.57	0.74 \pm 0.07	0.56	0.81 \pm 0.09	0.58	0.79 \pm 0.08	0.58
	VIRMOS-DESCART	1.02 \pm 0.08	0.60	0.98 \pm 0.08	0.59	1.05 \pm 0.08	0.62	1.03 \pm 0.09	0.61
	Combined	0.82 \pm 0.06	0.58	0.79 \pm 0.06	0.57	0.86 \pm 0.07	0.60	0.84 \pm 0.07	0.59

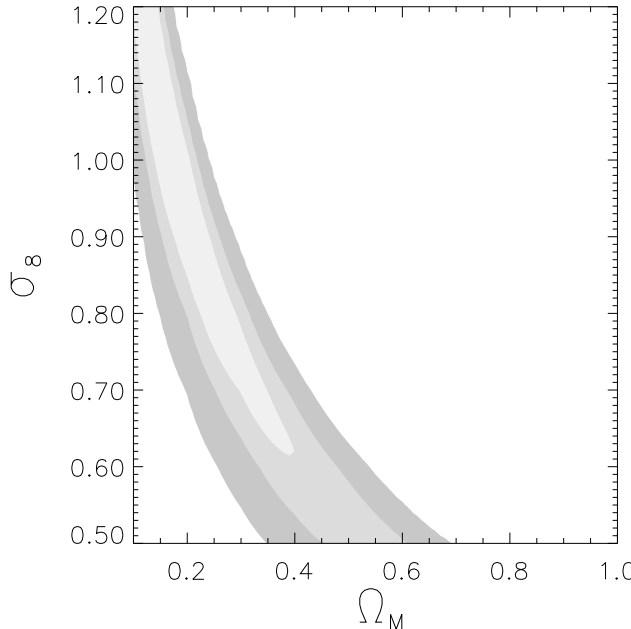


Figure 3. Joint constraints on σ_8 and Ω_m from the 100 deg 2 WL survey assuming a flat Λ CDM cosmology and adopting the non-linear matter power spectrum of Smith et al. (2003). The redshift distribution is estimated from the high confidence photometric redshift catalogue (Ilbert et al., 2006), and modeled with the standard functional form given by Eq.(9). The contours depict the 0.68, 0.95, and 0.99% confidence levels. The models are marginalised, over $h = 0.72 \pm 0.08$, shear calibration bias (see §4) with uniform priors, and the redshift distribution with Gaussian priors (see §6.1). Similar results are found for all other cases, as listed in Table 4.

$h \in [0.64, 0.80]$ with flat priors, $n(z)$ with Gaussian priors as described in §6.1, and a calibration bias of the shear signal with flat priors as discussed in §4. The corresponding constraints from each survey are presented in Figure 4 and tabulated in Table 4. Results in Table 4 are presented for two methods of calculating the non-linear power spectrum; Peacock & Dodds (1996) and Smith et al. (2003). We find a difference of approximately 3% in the best-fit σ_8 , where results using Smith et al. (2003) are consistently the smaller of the two. The contribution to the error budget due to the conservative addition of the B-modes to the covariance matrix is small, amounting to at most 0.01 in the 1σ error bar on σ_8 for an Ω_m of 0.24.

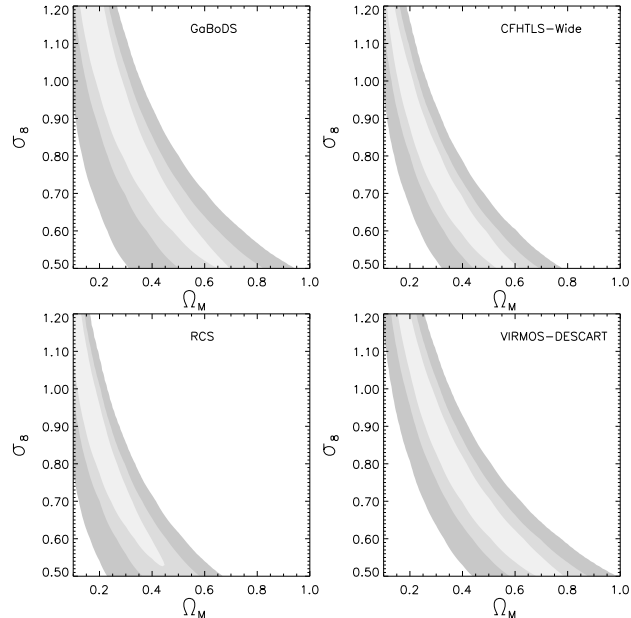


Figure 4. Joint constraints on σ_8 and Ω_m for each survey assuming a flat Λ CDM cosmology and adopting the non-linear matter power spectrum of Smith et al. (2003). The redshift distribution is estimated from the high confidence photometric redshift catalogue (Ilbert et al., 2006), and modeled with the standard functional form given by Eq.(9). The contours depict the 0.68, 0.95, and 0.99% confidence levels. The models are marginalised, over $h = 0.72 \pm 0.08$, shear calibration bias (see §4) with uniform priors, and the redshift distribution with Gaussian priors (see §6.1). Similar results are found for all other cases, as listed in Table 4.

We present a comparison of the measured σ_8 values with those previously published in Figure 5. The quoted σ_8 values are for an Ω_m of 0.24, and all error bars denote the 1σ region from the joint constraint contours. Our error bars (filled circles) are typically smaller than those from the literature (open circles) mainly due to the improved estimate of the redshift distribution. Our updated result for each survey agrees with the previous analysis within the error bars, this remains true if the literature values are lowered by $\sim 3\%$ to account for the difference in methods used for the non-linear power spectrum. Also plotted are the 1σ limits for the com-

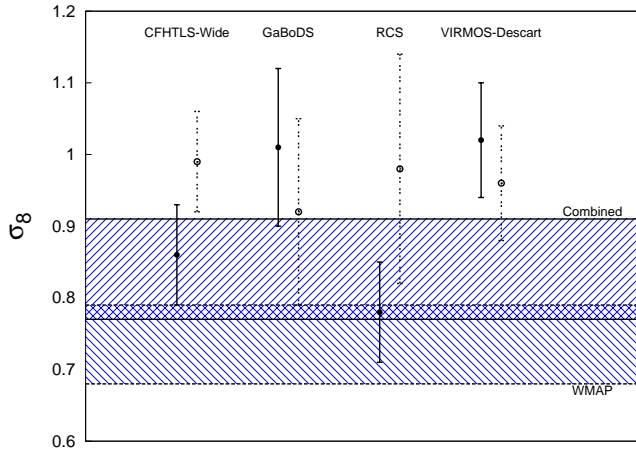


Figure 5. Values for σ_8 when Ω_m is taken to be 0.24, filled circles (solid) give our results with 1σ error bars, open circles (dashed) show the results from previous analyses (Table 1). Our results are given for the high confidence photometric redshift catalogue, using the functional form for $n(z)$ given by Eq.(9), and the Smith et al. (2003) prescription for the non-linear power spectrum. The literature values use the Peacock & Dodds (1996) prescription for non-linear power, and are expected to be $\sim 3\%$ higher than would be the case for Smith et al. (2003). The positively sloped hashed region (enclosed by solid lines) shows the 1σ range allowed by our combined result, the negatively sloped hashed region (enclosed by dashed lines) shows the 1σ range given by the WMAP 3 year results.

combined result and WMAP 3 year constraints (solid and dashed lines respectively), our result is consistent with WMAP at the 1σ level.

In addition to our main analysis we have investigated the impact of using four different models for the redshift distribution. These models are dependent on which functional form is used (Eq.(9) or Eq.(10)) and which range is used for the photometric redshift sample ($0.0 \leq z_p \leq 4.0$ or $0.2 \leq z_p \leq 1.5$). Table 4 gives the best fit joint constraints on σ_8 and Ω_m , for each survey as well as the combined survey result.

Comparing the best fit σ_8 values with the average redshifts listed in Table 2, we find, as expected, that higher redshift models result in lower values for σ_8 . Attempting to quantify this relation in terms of mean redshift fails. Changes in mean redshift are large ($\sim 14\%$) between the photometric samples, compared to $\sim 6\%$ between the two $n(z)$ models, however a $\sim 5\%$ change in σ_8 is seen for both. The median redshift is a much better gauge, changing by $\sim 4\%$ between both photometric samples and $n(z)$ models. Precision cosmology at the 1% level will necessitate roughly the same level of precision of the median redshift. Future cosmic shear surveys will require thorough knowledge of the complete redshift distribution of the sources, in particular to what extent a high redshift tail exists.

7 DISCUSSION AND CONCLUSION

We have performed an analysis of the 100 square degree weak lensing survey that combines four of the largest weak lensing datasets in existence. Our results provide the tightest weak lensing constraints on the amplitude of the matter power spectrum σ_8 and matter density Ω_m and a marked improvement on accuracy compared to previous results. Using the non-linear prediction of the cosmological power spectra given in Smith et al. (2003), the high confidence region of the photometric redshift calibra-

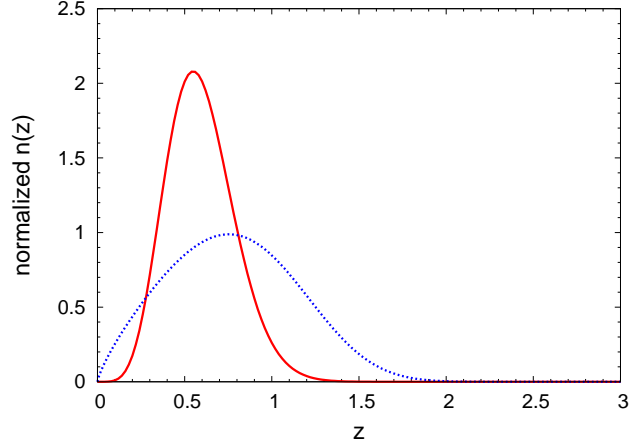


Figure 6. Redshift distributions for the RCS survey. The solid line shows the best fit $n(z)$ from Hoekstra et al. (2002a), the dashed curve is our best fit $n(z)$, the average redshifts are 0.6 and 0.78 respectively.

tion sample, and Eq.(9) to model the redshift distribution, we find $\sigma_8 = (0.84 \pm 0.07)(\frac{\Omega_m}{0.24})^{-0.59}$.

Our analysis differs from previous weak lensing analyses in three important aspects. We correctly account for non-Gaussian cosmic variance using the method of Semboloni et al. (2007), thus improving upon the purely Gaussian contribution given by Schneider et al. (2002). Using the results from STEP (Massey et al., 2007a) we correct for the shear calibration bias and marginalise over our uncertainty in this correction. In addition we use the largest deep photometric redshift catalogue in existence (Ilbert et al., 2006) to provide accurate models for the redshift distribution of sources, we also account for the effects of cosmic variance in these distributions (Van Waerbeke et al., 2006).

Accounting for the non-Gaussian contribution to the shear covariance matrix, which dominates on small scales, is very important. At a scale of 10 arcminutes the full non-Gaussian contribution is twice that of the Gaussian contribution alone, this discrepancy increases with decreasing scale, reaching an order of magnitude by 2 arcminutes. This increases the errors on the shear correlation function at small scales, leading to slightly weaker constraints on cosmology. Ideally we would estimate the shear covariance directly from the data, as is done in the previous analyses for both GaBoDS (Hettmansperger et al., 2006) and RCS (Hoekstra et al., 2002a). However, since we can not accomplish this for all the surveys in this work, due to a deficit of independent fields, we opt for a consistent approach by using the analytic treatment along with the non-Gaussian calibration as described in Semboloni et al. (2007).

Accurate determination of the redshift distribution of the sources is crucial for weak lensing cosmology since it is strongly degenerate with cosmological parameters. Past studies using small external photometric catalogues (such as the HDF) suffered from cosmic variance, a previously unquantified source of error that is taken into account here using the prescription of Van Waerbeke et al. (2006). In most cases the revised redshift distributions were in reasonable agreement with previous results, however this was not the case for the RCS survey. We found that the previous estimation was biased toward low redshift (see Figure 6), resulting in a significantly larger estimation of σ_8 ($0.86^{+0.04}_{-0.05}$ for $\Omega_m = 0.3$) than is presented here (0.69 ± 0.07). This difference is primarily due to a problem in the filter set conversion, between those used to image HDF (F300W, F450W, F606W, and F814W) and the Cousins R_C filter used by RCS.

In addition to using the best available photometric redshifts, we marginalise over the redshift distribution by selecting parameter triplets from their full 3D probability distribution, instead of fixing two parameters and varying the third as is often done. Thus the marginalisation is representative of the full range of $n(z)$ shapes, which are difficult to probe by varying one parameter due to degeneracies.

We have conducted our analysis using two different functional forms for the redshift distribution, the standard form given in Eq.(9) and a new form given by Eq.(10). The new function is motivated by the presence of a high- z tail when the entire photometric catalogue ($0.0 \leq z_p \leq 4.0$) is used to estimate the redshift distribution, Eq.(9) does a poor job of fitting this distribution (Figure 2). However when we restrict the photometric catalogue to the high confidence region ($0.2 \leq z_p \leq 1.5$) both functions fit well, and the tendency for Eq.(10) to exhibit a tail towards high- z increases the median redshift resulting in a slightly lower estimate of σ_8 . Though the tail of the distribution has only a small fraction of the total galaxies, they may have a significant lensing signal owing to their large redshifts. The influences of the different redshift distributions on cosmology is consistent within our 1σ errors but as survey sizes grow and statistical noise decreases, such differences will become significant. As the CFHTLS-Deep will be the largest deep photometric redshift catalogue for some years to come, this poses a serious challenge to future surveys attempting to do precision cosmology. To assess the extent of any high redshift tail, future surveys should strive to include photometric bands in the near infra-red, allowing for accurate redshift estimations beyond $z = 1.5$.

For $\Omega_m = 0.24$, the combined results using Eq.(9) are 0.80 ± 0.06 and 0.84 ± 0.07 for the unrestricted and high confidence photometric redshifts respectively, using Eq.(10) we find 0.77 ± 0.05 and 0.82 ± 0.06 (these results use the non-linear power spectrum given by Smith et al. (2003)). For completeness we provide results for both the Smith et al. (2003) and Peacock & Dodds (1996) non-linear power spectra, the resulting σ_8 values differ by $\sim 3\%$ of the Smith et al. (2003) value which is consistently the smaller of the two. As the Smith et al. (2003) study has been shown to be more accurate than Peacock & Dodds (1996), we prefer the results of this model, however, given the magnitude of variations resulting from different redshift distributions, this difference is not an important issue in the current work. However, accurately determining the non-linear matter power spectra is another challenge for future lensing surveys intent on precision cosmology. Alternatively, surveys focusing only on the large scale measurement of the shear (Fu et al., in prep.) are able to avoid complications arising from the estimation of non-linear power on small scales.

Surveys of varying depth provide different joint constraints in the $\Omega_m - \sigma_8$ plane, thus combining their likelihoods produces some degeneracy breaking. Taking the preferred prescription for the non-linear power spectrum, and using Eq.(9) along with the high confidence photometric redshifts to estimate the redshift distribution, we find an upper limit of $\Omega_m < \sim 0.4$ and a lower limit of $\sigma_8 > \sim 0.6$ both at the 1σ level (see Figure 3).

Our revised cosmological constraints introduce tension, at the $\sim 2\sigma$ level, between the results from the VIRIMOS-DESCART and RCS survey as shown in Figure 5. In this analysis we have accounted for systematic errors associated with shear measurement but have neglected potential systematics arising from correlations between galaxy shape and the underlying density field. This is valid in the case of intrinsic galaxy alignments which are expected to contribute less than a percent of the cosmic shear signal for the deep surveys used in this analysis (Heymans et al.,

2006b). What is currently uncertain however is the level of systematic error that arises from shear-ellipticity correlations (Hirata & Seljak, 2004; Heymans et al., 2006b; Mandelbaum et al., 2006; Hirata et al., 2007) which could reduce the amplitude of the measured shear correlation function by $\sim 10\%$ (Heymans et al., 2006b). It has been found from the analysis of the Sloan Digital Sky Survey (Mandelbaum et al., 2006; Hirata et al., 2007), that different morphological galaxy types contribute differently to this effect. It is therefore possible that the different R-band imaging of the RCS and the slightly lower median survey redshift make it more susceptible to this type of systematic error. Without complete redshift information for each survey, however, it is not possible to test this hypothesis or to correct for this potential source of error. In the future deep multi-colour data will permit further investigation and correction for this potential source of systematic error.

Weak lensing by large scale structure is an excellent means of constraining cosmology. The unambiguous interpretation of the shear signal allows for a direct measure of the dark matter power spectrum, allowing for a unique and powerful means of constraining cosmology. Our analysis has shown that accurately describing the redshift distribution of the sources is vital to future surveys intent on precision cosmology. Including near-IR bands to photometric redshift estimates will be a crucial step in achieving this goal, allowing for reliable redshift estimates at $z > 1.5$ and assessing the extent of a high- z tail.

ACKNOWLEDGMENTS

JB is supported by the Natural Sciences and Engineering Research Council (NSERC), and the Canadian Institute for Advanced Research (CIAR). CH acknowledges the support of the European Commission Programme 6th frame work, Marie Curie Outgoing International Fellowship, contract number M01F-CT-2006-21891, and a CITA National Fellowship. ES thanks the hospitality of the University of British Columbia, which made this collaboration possible. LVW and HH are supported by NSERC, CIAR and the Canadian Foundation for Innovation (CFI). YM thanks the Alexander Humboldt Foundation and the Terapix data center for support, and the AIfA for hospitality. This work is partly based on observations obtained with MegaPrime equipped with MegaCam, a joint project of CFHT and CEA/DAPNIA, at the Canada-France-Hawaii Telescope (CFHT) which is operated by the National Research Council (NRC) of Canada, the Institut National des Sciences de l'Univers of the Centre National de la Recherche Scientifique (CNRS) of France, and the University of Hawaii. This work is based in part on data products produced at TERAPIX and the Canadian Astronomy Data Centre as part of the Canada-France-Hawaii Telescope Legacy Survey, a collaborative project of NRC and CNRS. This research was performed with infrastructure funded by the Canadian Foundation for Innovation and the British Columbia Knowledge Development Fund (A Parallel Computer for Compact-Object Physics). This research has been enabled by the use of WestGrid computing resources, which are funded in part by the Canada Foundation for Innovation, Alberta Innovation and Science, BC Advanced Education, the participating research institutions. WestGrid equipment is provided by IBM, Hewlett Packard and SGI.

Table A1. E and B modes of the shear correlation function for the CFHTLS-Wide survey, the error ($\delta\xi$) is statistical only, and given as the standard deviation.

θ	ξ_E	ξ_B	$\delta\xi$
0.74	1.53060e-04	-4.16557e-05	2.31000e-05
1.44	1.00161e-04	1.79443e-05	1.22000e-05
2.37	5.82357e-05	-1.60557e-05	9.64000e-06
3.54	3.11136e-05	7.14429e-06	6.66000e-06
5.41	2.89396e-05	-2.05571e-06	4.29000e-06
7.28	3.08030e-05	-3.47571e-06	4.76000e-06
8.69	1.41053e-05	6.14429e-06	4.43000e-06
11.72	1.66208e-05	-5.15714e-07	2.16000e-06
18.74	1.50680e-05	4.14286e-07	1.25000e-06
28.09	1.07719e-05	-7.95715e-07	1.03000e-06
37.44	8.72227e-06	4.14286e-07	9.10000e-07
49.12	8.11150e-06	-2.18571e-06	6.64000e-07
62.92	8.97071e-06	-3.01571e-06	6.25000e-07

Table A2. E and B modes of the shear correlation function for GaBoDS, the error ($\delta\xi$) is statistical only, and given as the standard deviation.

θ	ξ_E	ξ_B	$\delta\xi$
0.36	2.80637e-04	1.38754e-04	9.54000e-05
0.50	1.72930e-04	1.24754e-04	6.92000e-05
0.70	1.15363e-04	6.74540e-05	4.99000e-05
0.98	1.20006e-04	-1.59760e-05	3.81000e-05
1.36	8.75079e-05	2.76540e-05	2.80000e-05
1.90	7.43231e-05	8.35400e-06	2.15000e-05
2.65	9.55859e-05	-2.30860e-05	1.71000e-05
3.69	6.48524e-05	3.05400e-06	1.40000e-05
5.16	4.30325e-05	5.25400e-06	1.19000e-05
7.19	2.73408e-05	-7.24600e-06	1.03000e-05
10.03	9.97772e-06	-7.46000e-07	8.65000e-06
13.99	1.22154e-05	-6.54600e-06	6.55000e-06

APPENDIX A: ADDITIONAL DATA

Here we present both the measured shear correlation function and the covariance matrix for each survey. The shear correlation function, given in Tables A1, A2, A3 and A4 for the CFHTLS-Wide, GaBoDS, RCS and VIRMOS-DESCART surveys respectively, has been calibrated on large scales where $\langle M_{\text{ap}}^2(\Delta\theta) \rangle_{\perp}$ is consistent with zero as described in §4.

Tables A5, A6, A7 and A8 for the CFHTLS-Wide, GaBoDS, RCS and VIRMOS-DESCART surveys respectively tabulate the correlation coefficient matrix:

$$\mathbf{C}_{ij} = \frac{\mathbf{C}_{ij}}{\langle \xi_i^2 \rangle^{1/2} \langle \xi_j^2 \rangle^{1/2}}, \quad (\text{A1})$$

where \mathbf{C} is the covariance matrix, as described in §6 for each survey. We also tabulate $\langle \xi_i^2 \rangle$ so that the covariance matrix may be calculated from the correlation coefficient matrix. Note that $\langle \xi_i^2 \rangle$ is the variance of the i^{th} scale, equivalent to \mathbf{C}_{ii} .

References

Astier P., Guy J., Regnault N., Pain R., Aubourg E., Balam D.,

Table A3. E and B modes of the shear correlation function for RCS, the error ($\delta\xi$) is statistical only, and given as the standard deviation.

θ	ξ_E	ξ_B	$\delta\xi$
1.12	9.71718e-05	2.78320e-05	1.99000e-05
1.75	3.38178e-05	1.67320e-05	1.91000e-05
2.50	3.74410e-05	4.00200e-06	1.16000e-05
3.24	4.27205e-05	6.63200e-06	1.43000e-05
4.00	1.49772e-05	1.58320e-05	9.21000e-06
5.75	1.52878e-05	-8.80000e-08	5.13000e-06
8.50	1.50807e-05	-3.89600e-06	3.95000e-06
12.25	6.89234e-06	2.15200e-06	2.85000e-06
16.49	4.81573e-06	1.83200e-06	2.65000e-06
20.74	4.69151e-06	1.82200e-06	2.30000e-06
26.49	5.29607e-06	3.59200e-06	1.75000e-06
34.99	5.33747e-06	1.11200e-06	1.36000e-06
46.49	6.91304e-06	-4.88000e-07	1.08000e-06
56.51	6.69565e-06	-4.88000e-07	1.34000e-06

Table A4. E and B modes of the shear correlation function for the VIRMOS-DESCART survey, the error ($\delta\xi$) is statistical only, and given as the standard deviation.

θ	ξ_E	ξ_B	$\delta\xi$
0.73	2.26695e-04	3.91133e-05	3.98000e-05
1.05	1.69759e-04	-1.59667e-06	3.90000e-05
1.51	1.30421e-04	5.31333e-06	2.20000e-05
2.29	9.60525e-05	2.82133e-05	1.57000e-05
3.20	6.60318e-05	-1.38767e-05	1.35000e-05
4.11	5.56798e-05	6.41333e-06	1.22000e-05
5.02	5.29883e-05	3.71333e-06	1.12000e-05
6.39	3.50794e-05	-1.26667e-06	7.46000e-06
8.21	1.94893e-05	2.11333e-06	6.75000e-06
11.41	2.72119e-05	-8.46667e-07	3.99000e-06
15.97	1.98620e-05	4.81333e-06	3.50000e-06
20.53	1.67357e-05	5.41333e-06	3.23000e-06
25.25	1.05659e-05	4.51333e-06	2.95000e-06
30.23	9.77399e-06	1.31333e-06	2.73000e-06
35.10	1.06073e-05	-1.05667e-06	2.71000e-06
39.78	1.17771e-05	-2.08667e-06	2.61000e-06

Basa S., Carlberg R. G., Fabbro S., Fouchez D., Hook I. M., Howell D. A., Lafoux H., Neill J. D., Palanque-Delabrouille N., Perrett K., Pritchett C. J., Rich J., Sullivan M., Taillet R., Aldering G., Antilogus P., Arsenijevic V., Balland C., Baumont S., Brion J., Courtois H., Ellis R. S., Filiol M., Gonçalves A. C., Goobar A., Guide D., Hardin D., Lusset V., Lidman C., McMahon R., Mouchet M., Mourao A., Perlmuter S., Ripoche P., Tao C., Walton N., 2006, A&A, 447, 31
 Bacon D. J., Massey R. J., Refregier A. R., Ellis R. S., 2003, MNRAS, 344, 673
 Bacon D. J., Refregier A. R., Ellis R. S., 2000, MNRAS, 318, 625
 Bacon D. J., Taylor A. N., Brown M. L., Gray M. E., Wolf C., Meisenheimer K., Dye S., Wisotzki L., Borch A., Kleinheinrich M., 2005, MNRAS, 363, 723
 Bartelmann M., Schneider P., 2001, Phys. Rep., 340, 291
 Blanton M. R., Roweis S., 2007, AJ, 133, 734
 Brown M. L., Taylor A. N., Bacon D. J., Gray M. E., Dye S., Meisenheimer K., Wolf C., 2003, MNRAS, 341, 100

Table A5. The correlation coefficient matrix (\mathbf{r}) for the CFHTLS-Wide survey, the scales θ_i correspond to those given in Table A1. The column $\langle \xi_i^2 \rangle$ is given in units of 10^{-10} , and can be used to reconstruct the covariance matrix \mathbf{C} .

$\langle \xi_i^2 \rangle$	θ_1	θ_2	θ_3	θ_4	θ_5	θ_6	θ_7	θ_8	θ_9	θ_{10}	θ_{11}	θ_{12}	θ_{13}	
θ_1	29.92	1.00	0.26	0.18	0.20	0.21	0.11	0.06	0.07	0.07	0.06	0.05	0.04	0.03
θ_2	6.60	0.26	1.00	0.22	0.24	0.25	0.16	0.11	0.15	0.14	0.13	0.12	0.08	0.06
θ_3	4.26	0.18	0.22	1.00	0.22	0.23	0.16	0.12	0.19	0.18	0.16	0.15	0.10	0.07
θ_4	1.35	0.20	0.24	0.22	1.00	0.35	0.25	0.21	0.34	0.32	0.28	0.26	0.19	0.13
θ_5	0.44	0.21	0.25	0.23	0.35	1.00	0.42	0.37	0.61	0.56	0.48	0.45	0.32	0.22
θ_6	0.56	0.11	0.16	0.16	0.25	0.42	1.00	0.34	0.55	0.49	0.42	0.40	0.29	0.19
θ_7	0.81	0.06	0.11	0.12	0.21	0.37	0.34	1.00	0.47	0.41	0.35	0.33	0.24	0.16
θ_8	0.25	0.07	0.15	0.19	0.34	0.61	0.55	0.47	1.00	0.75	0.63	0.60	0.43	0.29
θ_9	0.18	0.07	0.14	0.18	0.32	0.56	0.49	0.41	0.75	1.00	0.78	0.71	0.51	0.35
θ_{10}	0.14	0.06	0.13	0.16	0.28	0.48	0.42	0.35	0.63	0.78	1.00	0.82	0.57	0.39
θ_{11}	0.11	0.05	0.12	0.15	0.26	0.45	0.40	0.33	0.60	0.71	0.82	1.00	0.69	0.45
θ_{12}	0.13	0.04	0.08	0.10	0.19	0.32	0.29	0.24	0.43	0.51	0.57	0.69	1.00	0.42
θ_{13}	0.16	0.03	0.06	0.07	0.13	0.22	0.19	0.16	0.29	0.35	0.39	0.45	0.42	1.00

Table A6. The correlation coefficient matrix (\mathbf{r}) for GaBoDS, the scales θ_i correspond to those given in Table A2. The column $\langle \xi_i^2 \rangle$ is given in units of 10^{-10} , and can be used to reconstruct the covariance matrix \mathbf{C} .

	$\langle \xi_i^2 \rangle$	θ_1	θ_2	θ_3	θ_4	θ_5	θ_6	θ_7	θ_8	θ_9	θ_{10}	θ_{11}	θ_{12}
θ_1	323.76	1.00	0.12	0.13	0.17	0.14	0.16	0.10	0.14	0.11	0.09	0.09	0.06
θ_2	223.36	0.12	1.00	0.12	0.16	0.12	0.15	0.10	0.13	0.11	0.09	0.09	0.06
θ_3	80.29	0.13	0.12	1.00	0.21	0.16	0.19	0.13	0.18	0.16	0.13	0.14	0.09
θ_4	22.13	0.17	0.16	0.21	1.00	0.25	0.30	0.20	0.29	0.25	0.22	0.23	0.15
θ_5	18.26	0.14	0.12	0.16	0.25	1.00	0.28	0.19	0.28	0.25	0.22	0.23	0.17
θ_6	6.91	0.16	0.15	0.19	0.30	0.28	1.00	0.28	0.42	0.38	0.33	0.37	0.27
θ_7	9.21	0.10	0.10	0.13	0.20	0.19	0.28	1.00	0.34	0.32	0.28	0.32	0.23
θ_8	2.67	0.14	0.13	0.18	0.29	0.28	0.42	0.34	1.00	0.58	0.53	0.59	0.42
θ_9	2.20	0.11	0.11	0.16	0.25	0.25	0.38	0.32	0.58	1.00	0.58	0.64	0.46
θ_{10}	2.01	0.09	0.09	0.13	0.22	0.22	0.33	0.28	0.53	0.58	1.00	0.66	0.47
θ_{11}	1.13	0.09	0.09	0.14	0.23	0.23	0.37	0.32	0.59	0.64	0.66	1.00	0.61
θ_{12}	1.20	0.06	0.06	0.09	0.15	0.17	0.27	0.23	0.42	0.46	0.47	0.61	1.00

Table A7. The correlation coefficient matrix (\mathbf{r}) for RCS, the scales θ_i correspond to those given in Table A3. The column $\langle \xi_i^2 \rangle$ is given in units of 10^{-10} , and can be used to reconstruct the covariance matrix \mathbf{C} .

$\langle \xi_i^2 \rangle$	θ_1	θ_2	θ_3	θ_4	θ_5	θ_6	θ_7	θ_8	θ_9	θ_{10}	θ_{11}	θ_{12}	θ_{13}	θ_{14}	
θ_1	12.95	1.00	0.10	0.13	0.08	0.05	0.11	0.07	0.07	0.06	0.06	0.04	0.05	0.05	0.04
θ_2	7.03	0.10	1.00	0.14	0.08	0.06	0.12	0.08	0.09	0.08	0.08	0.06	0.07	0.07	0.05
θ_3	1.84	0.13	0.14	1.00	0.14	0.10	0.21	0.16	0.17	0.16	0.15	0.11	0.14	0.13	0.10
θ_4	2.74	0.08	0.08	0.14	1.00	0.08	0.17	0.13	0.14	0.13	0.13	0.09	0.12	0.10	0.08
θ_5	3.56	0.05	0.06	0.10	0.08	1.00	0.15	0.11	0.12	0.12	0.11	0.08	0.10	0.09	0.07
θ_6	0.42	0.11	0.12	0.21	0.17	0.15	1.00	0.35	0.36	0.34	0.32	0.23	0.29	0.27	0.21
θ_7	0.44	0.07	0.08	0.16	0.13	0.11	0.35	1.00	0.38	0.34	0.32	0.23	0.29	0.26	0.21
θ_8	0.24	0.07	0.09	0.17	0.14	0.12	0.36	0.38	1.00	0.49	0.42	0.31	0.40	0.36	0.29
θ_9	0.19	0.06	0.08	0.16	0.13	0.12	0.34	0.34	0.49	1.00	0.49	0.35	0.45	0.41	0.33
θ_{10}	0.17	0.06	0.08	0.15	0.13	0.11	0.32	0.32	0.42	0.49	1.00	0.38	0.48	0.44	0.35
θ_{11}	0.23	0.04	0.06	0.11	0.09	0.08	0.23	0.23	0.31	0.35	0.38	1.00	0.45	0.38	0.30
θ_{12}	0.08	0.05	0.07	0.14	0.12	0.10	0.29	0.29	0.40	0.45	0.48	0.45	1.00	0.66	0.51
θ_{13}	0.06	0.05	0.07	0.13	0.10	0.09	0.27	0.26	0.36	0.41	0.44	0.38	0.66	1.00	0.64
θ_{14}	0.05	0.04	0.05	0.10	0.08	0.07	0.21	0.21	0.29	0.33	0.35	0.30	0.51	0.64	1.00

Table A8. The correlation coefficient matrix (\mathbf{r}) for the VIRMOS-DESCART survey, the scales θ_i correspond to those given in Table A4. The column $\langle \xi_i^2 \rangle$ is given in units of 10^{-10} , and can be used to reconstruct the covariance matrix \mathbf{C} .

$\langle \xi_i^2 \rangle$	θ_1	θ_2	θ_3	θ_4	θ_5	θ_6	θ_7	θ_8	θ_9	θ_{10}	θ_{11}	θ_{12}	θ_{13}	θ_{14}	θ_{15}	θ_{16}
θ_1	46.55	1.00	0.35	0.37	0.19	0.21	0.22	0.20	0.19	0.16	0.14	0.08	0.06	0.06	0.07	0.06
θ_2	23.02	0.35	1.00	0.40	0.20	0.22	0.24	0.22	0.21	0.17	0.15	0.10	0.09	0.09	0.10	0.09
θ_3	8.92	0.37	0.40	1.00	0.26	0.28	0.28	0.26	0.26	0.22	0.21	0.17	0.15	0.14	0.15	0.13
θ_4	12.17	0.19	0.20	0.26	1.00	0.19	0.19	0.17	0.18	0.17	0.18	0.14	0.13	0.12	0.13	0.11
θ_5	4.76	0.21	0.22	0.28	0.19	1.00	0.26	0.25	0.28	0.27	0.29	0.23	0.20	0.20	0.21	0.20
θ_6	2.69	0.22	0.24	0.28	0.19	0.26	1.00	0.35	0.39	0.36	0.38	0.30	0.27	0.26	0.28	0.24
θ_7	2.11	0.20	0.22	0.26	0.17	0.25	0.35	1.00	0.45	0.42	0.43	0.33	0.30	0.29	0.31	0.27
θ_8	1.26	0.19	0.21	0.26	0.18	0.28	0.39	0.45	1.00	0.55	0.56	0.44	0.39	0.38	0.41	0.35
θ_9	1.08	0.16	0.17	0.22	0.17	0.27	0.36	0.42	0.55	1.00	0.64	0.49	0.43	0.41	0.44	0.38
θ_{10}	0.68	0.14	0.15	0.21	0.18	0.29	0.38	0.43	0.56	0.64	1.00	0.64	0.52	0.52	0.56	0.48
θ_{11}	0.77	0.08	0.10	0.17	0.14	0.23	0.30	0.33	0.44	0.49	0.64	1.00	0.49	0.49	0.53	0.51
θ_{12}	0.80	0.06	0.09	0.15	0.13	0.20	0.27	0.30	0.39	0.43	0.52	0.49	1.00	0.50	0.53	0.51
θ_{13}	0.62	0.06	0.09	0.14	0.12	0.20	0.26	0.29	0.38	0.41	0.52	0.49	0.50	1.00	0.63	0.60
θ_{14}	0.41	0.07	0.10	0.15	0.13	0.21	0.28	0.31	0.41	0.44	0.56	0.53	0.53	0.63	1.00	0.74
θ_{15}	0.34	0.06	0.09	0.15	0.13	0.20	0.27	0.30	0.39	0.42	0.54	0.51	0.51	0.60	0.74	1.00
θ_{16}	0.35	0.06	0.08	0.13	0.11	0.18	0.24	0.27	0.35	0.38	0.48	0.46	0.45	0.52	0.65	0.70
																1.00

Crittenden R. G., Natarajan P., Pen U.-L., Theuns T., 2001, ApJ, 559, 552

Crittenden R. G., Natarajan P., Pen U.-L., Theuns T., 2002, ApJ, 568, 20

Freedman W. L., Madore B. F., Gibson B. K., Ferrarese L., Kelson D. D., Sakai S., Mould J. R., Kennicutt Jr. R. C., Ford H. C., Graham J. A., Huchra J. P., Hughes S. M. G., Illingworth G. D., Macri L. M., Stetson P. B., 2001, ApJ, 553, 47

Fukugita M., Ichikawa T., Gunn J. E., Doi M., Shimasaku K., Schneider D. P., 1996, AJ, 111, 1748

Hamana T., Miyazaki S., Shimasaku K., Furusawa H., Doi M., Hamabe M., Imi K., Kimura M., Komiyama Y., Nakata F., Okada N., Okamura S., Ouchi M., Sekiguchi M., Yagi M., Yasuda N., 2003, ApJ, 597, 98

Hetterscheidt M., Simon P., Schirmer M., Hildebrandt H., Schrabback T., Erben T., Schneider P., 2006, preprint astro-ph/0606571

Heymans C., Brown M. L., Barden M., Caldwell J. A. R., Jahnke K., Peng C. Y., Rix H.-W., Taylor A., Beckwith S. V. W., Bell E. F., Borch A., Häufner B., Jogee S., McIntosh D. H., Meisenheimer K., Sánchez S. F., Somerville R., Wisotzki L., Wolf C., 2005, MNRAS, 361, 160

Heymans C., Van Waerbeke L., Bacon D., Berge J., Bernstein G., Bertin E., Bridle S., Brown M. L., Clowe D., Dahle H., Erben T., Gray M., Hetterscheidt M., Hoekstra H., Hudelot P., Jarvis M., Kuijken K., Margoniner V., Massey R., Mellier Y., Nakajima R., Refregier A., Rhodes J., Schrabback T., Wittman D., 2006a, MNRAS, 368, 1323

Heymans C., White M., Heavens A., Vale C., Van Waerbeke L., 2006b, MNRAS, 371, 750

Hirata C. M., Mandelbaum R., Ishak M., Seljak U., Nichol R., Pimbblet K. A., Ross N. P., Wake D., 2007, preprint astro-ph/0701671

Hirata C. M., Seljak U., 2004, 70

Hoekstra H., Franx M., Kuijken K., Squires G., 1998, New Astronomy Review, 42, 137

Hoekstra H., Mellier Y., Van Waerbeke L., Semboloni E., Fu L., Hudson M. J., Parker L. C., Tereno I., Benabed K., 2006, ApJ, 647, 116

Hoekstra H., Yee H. K. C., Gladders M. D., 2002a, ApJ, 577, 595

Hoekstra H., Yee H. K. C., Gladders M. D., Barrientos L. F., Hall P. B., Infante L., 2002b, ApJ, 572, 55

Ilbert O., Arnouts S., McCracken H. J., Bolzonella M., Bertin E., Le Fèvre O., Mellier Y., Zamorani G., Pellò R., Iovino A., Tresse L., Le Brun V., Bottini D., Garilli B., Maccagni D., Piscat J. P., Scaramella R., Scovelli M., Vettolani G., Zanichelli A., Adami C., Bardelli S., Cappi A., Charlot S., Ciliegi P., Contini T., Cucciati O., Foucaud S., Franzetti P., Gavignaud I., Guzzo L., Marano B., Marinoni C., Mazure A., Meneux B., Merighi R., Paltani S., Pollo A., Pozzetti L., Radovich M., Zucca E., Bondi M., Bongiorno A., Busarello G., de La Torre S., Gregorini L., Lamareille F., Mathez G., Merluzzi P., Ripepi V., Rizzo D., Vergani D., 2006, A&A, 457, 841

Jarvis M., Bernstein G. M., Fischer P., Smith D., Jain B., Tyson J. A., Wittman D., 2003, AJ, 125, 1014

Jarvis M., Jain B., Bernstein G., Dolney D., 2006, ApJ, 644, 71

Kaiser N., Squires G., Broadhurst T., 1995, ApJ, 449, 460

Kaiser N., Wilson G., Luppino G. A., 2000, preprint astro-ph/0003338

Kitching T. D., Heavens A. F., Taylor A. N., Brown M. L., Meisenheimer K., Wolf C., Gray M. E., Bacon D. J., 2006, preprint astro-ph/0610284

Le Fèvre O., Mellier Y., McCracken H. J., Foucaud S., Gwyn S., Radovich M., Dantel-Fort M., Bertin E., Moreau C., Cuillandre J.-C., Pierre M., Le Brun V., Mazure A., Tresse L., 2004, A&A, 417, 839

Luppino G. A., Kaiser N., 1997, ApJ, 475, 20

Mandelbaum R., Hirata C. M., Ishak M., Seljak U., Brinkmann J., 2006, 367, 611

Massey R., Heymans C., Bergé J., Bernstein G., Bridle S., Clowe D., Dahle H., Ellis R., Erben T., Hetterscheidt M., High F. W., Hirata C., Hoekstra H., Hudelot P., Jarvis M., Johnston D., Kuijken K., Margoniner V., Mandelbaum R., Mellier Y., Nakajima R., Paulin-Henriksson S., Peebles M., Roat C., Refregier A., Rhodes J., Schrabback T., Schirmer M., Seljak U., Semboloni E., Van Waerbeke L., 2007a, MNRAS, 376, 13

Massey R., Refregier A., Bacon D. J., Ellis R., Brown M. L., 2005, MNRAS, 359, 1277

Massey R., Rhodes J., Leauthaud A., Capak P., Ellis R., Koekemoer A., Refregier A., Scoville N., Taylor J. E., Albert J., Berge J., Heymans C., Johnston D., Kneib J.-P., Mellier Y., Mobasher B., Semboloni E., Shopbell P., Tasca L., Van Waerbeke L., 2007b, preprint astro-ph/0701480

McCracken H. J., Radovich M., Bertin E., Mellier Y., Dantel-Fort M., Le Fèvre O., Cuillandre J. C., Gwyn S., Foucaud S., Zamorani G., 2003, *A&A*, 410, 17

Munshi D., Valageas P., Van Waerbeke L., Heavens A., 2006, preprint astro-ph/0612667

Peacock J. A., Dodds S. J., 1996, *MNRAS*, 280, L19

Pen U.-L., Van Waerbeke L., Mellier Y., 2002, *ApJ*, 567, 31

Rhodes J., Refregier A., Collins N. R., Gardner J. P., Groth E. J., Hill R. S., 2004, *ApJ*, 605, 29

Schneider P., Van Waerbeke L., Jain B., Kruse G., 1998, *MNRAS*, 296, 873

Schneider P., Van Waerbeke L., Kilbinger M., Mellier Y., 2002, *A&A*, 396, 1

Schrabback T., Erben T., Simon P., Miralles J. , Schneider P., Heymans C., Eifler T., Fosbury R. A. E., Freudling W., Hetterscheidt M., Hildebrandt H., Pirzkal N., 2006, preprint astro-ph/0606611

Semboloni E., Mellier Y., Van Waerbeke L., Hoekstra H., Tereno I., Benabed K., Gwyn S. D. J., Fu L., Hudson M. J., Maoli R., Parker L. C., 2006, *A&A*, 452, 51

Semboloni E., Van Waerbeke L., Heymans C., Hamana T., Colombi S., White M., Mellier Y., 2007, *MNRAS*, 375, L6

Smith R. E., Peacock J. A., Jenkins A., White S. D. M., Frenk C. S., Pearce F. R., Thomas P. A., Efstathiou G., Couchman H. M. P., 2003, *MNRAS*, 341, 1311

Spergel D. N., Bean R., Doré O., Nolta M. R., Bennett C. L., Dunkley J., Hinshaw G., Jarosik N., Komatsu E., Page L., Peiris H. V., Verde L., Halpern M., Hill R. S., Kogut A., Limon M., Meyer S. S., Odegard N., Tucker G. S., Weiland J. L., Wollack E., Wright E. L., 2006, ArXiv Astrophysics e-prints

Van Waerbeke L., Mellier Y., Erben T., Cuillandre J. C., Bernardeau F., Maoli R., Bertin E., McCracken H. J., Le Fèvre O., Fort B., Dantel-Fort M., Jain B., Schneider P., 2000, *A&A*, 358, 30

Van Waerbeke L., Mellier Y., Hoekstra H., 2005, *A&A*, 429, 75

Van Waerbeke L., Mellier Y., Pelló R., Pen U.-L., McCracken H. J., Jain B., 2002, *A&A*, 393, 369

Van Waerbeke L., Mellier Y., Radovich M., Bertin E., Dantel-Fort M., McCracken H. J., Le Fèvre O., Foucaud S., Cuillandre J.-C., Erben T., Jain B., Schneider P., Bernardeau F., Fort B., 2001, *A&A*, 374, 757

Van Waerbeke L., White M., Hoekstra H., Heymans C., 2006, *Astroparticle Physics*, 26, 91

Wall J. V., Jenkins C. R., 2003, *Practical Statistics for Astronomers*. Princeton Series in Astrophysics

Wittman D., 2005, *ApJ*, 632, L5

Wittman D. M., Tyson J. A., Kirkman D., Dell'Antonio I., Bernstein G., 2000, *Nature*, 405, 143